Facile in-situ synthesis of freestanding 3D nanoporous Cu@Cu_2O hierarchical nanoplate arrays as binder-free integrated anodes for high-capacity, long-life Li-ion batteries

Wenbo Liu,[a,*] Peng Cheng,[a] Shichao Zhang,[b] and Sanqiang Shi[c]

[a] School of Mechanical Engineering, Sichuan University, Chengdu 610065, China

[b] School of Materials Science and Engineering, Beihang University, Beijing 100191, China

[c] Department of Mechanical Engineering, The Hong Kong Polytechnic University, Hung Hom, Kowloon, Hong Kong

Tel: +86-028-85405320; Fax: +86-028-85403408; E-mail: liuwenbo_8338@163.com.

Freestanding 3D nanoporous Cu supported Cu_2O hierarchical nanoplate arrays (3D NPC@Cu_2O HNPAs) have been prepared in-situ by facile one-step oxidation-assisted electrochemical dealloying, in which Cu_2O HNPAs is characteristic of large-sized (hundreds of nm) 2D nanoplate arrays firmly embedded in small-sized (tens of nm) counterparts. The unique 3D nanocomposites as anodes for Li-ion batteries (LIBs) display superior Li storage properties involving ultrahigh specific capacity, long cycle life and excellent rate capability, which deliver a reversible capacity as high as 3.0 mAh cm^{-2} with 71.4% capacity retention after 450 long-cycles at 2 mA cm^{-2}. Even when the current density reaches 5 mA cm^{-2}, an ultrahigh reversible capacity of 3.4 mAh cm^{-2} still can be achieved smoothly without obvious capacity decay after 250 cycles. It is totally comparable to or even exceeds the current level of commercial graphite anode. The outstanding electrochemical performance can be largely ascribed to the unique 3D electrode structure comprising HNPAs and NP substrate, large contact area between active material and electrolyte, in-situ growth of active material upon porous substrate, compact joint of small-sized intermediate nanolayers, and favorable mass transfer amongst vertical hierarchical nanoplates, indicative of a quite promising candidate as a binder-free integrated anode toward practical application of advanced LIBs.

Keywords: *Li-ion battery; In-situ synthesis; Dealloying; Hierarchical nanoplate arrays; Anode*

I. INTRODUCTION

NOWADAYS, with the rapid development of industry and society, the excessive depletion of fossil fuels and increasing environment pollutions have become focus issues in human life, while green, clean and sustainable energy strategy is a valid solution. Li-ion battery, as a new kind of renewable energy storage device, can be expected to overcome the above-mentioned challenges effectively due to its high energy/power density, long cycle life, environment benignity, renewable utilization, and so on.[1-4] However, graphite anode widely used in currently commercial LIBs is seemingly difficult to meet the future-oriented demands in rechargable electrical vehicles and smart power grids in view of its inherent limitations in low theoretical specific capacity (372 mAh g^{-1}), unsatisfactory rate capability and poor safety.[5-6] As a result, seeking high-performance anode materials is imperative. In recent years, transition metal oxides (TMOs, M=Fe, Mn, Co, Cu, etc.) with multi-electron conversion reactions proposed by Tarascon et al. have attracted considerable attention owing to higher specific capacity, longer cycle life and better rate ability.[7] Among them, Cu_2O is one of the most promising anode candidates in consideration of its unique physical characteristics, such as high safety, low cost, nontoxicity and abundant sources. Even so, there still exist many obvious drawbacks that need to be solved urgently before commercialization, especially for low electrical conductivity and rapid exfoliation of active materials caused by violent volume and structure changes during repeated electrochemical reactions, which would markedly reduce charge transport ability and thus lead to poor Li storage properties.[8]

To decrease the negative volume effects and improve the overall electrochemical performance, various Cu_2O anodes with different nanostructure designs have been synthesized and probed widely in LIBs, such as nanoparticles,[9] nanorods,[10,11] nanowires,[12] nanospheres,[13] and nanoplates.[14,15] Among them, 2D nanoplate array structure can attract greater interests due to their large specific surface areas, unique charge transport pathways and multi-coupling quantum effects, leading to the improved electrochemical performance. For example, Song et al.[15] reported the 2D planar copper foil supported Cu_2O nanoplate arrays fabricated by potentiodynamic electrodeposition, which exhibited gradually increasing reversible capacities from 323 to 1206 mAh g^{-1} during 500 cycles. Obviously, compared to conventional 2D planar counterparts, 3D nanostructured substrates greatly facilitate to enhance permeability of organic electrolytes, as well as buffer huge volume and structure changes during repeated charge-discharge processes, achieving enhanced Li storage properties.[16] Typically, 3D nanoporous (NP) metals, being able to act as both current collector and substrate of active materials simultaneously, have many unique advantages towards application of LIBs, such as robust 3D skeleton, large contact surface area, good electrical conductivity, high electrochemical active sites and fast ion/electron transfer ability. As a result, integrating 3D NP substrate and 2D Cu_2O nanoplate arrays might be a more rational and high-efficient strategy to further boost Li storage performance. Generally, template method can be used to prepare various 3D NP electrodes for LIBs, but it is always sophisticated, time-consuming and high-polluting, which would bring about a tough challenge for large-scale production in the industry.[17-21] Recently,

dealloying has been proved to be a simple and effective route to obtain diverse 3D NP structures, which has obvious merits of simple processing, nearly absolute yield, and being applicable for large-scale synthesis.[22-24] Nevertheless, at present, there are few reports on successful preparation of 3D NP/2D nanoplate array integrated structure by effective dealloying. Besides, in commercial electrodes, the widespread uses of poly(vinylidene fluoride) (PVDF) as an organic binder and acetylene black as a conductive agent largely tend to decrease energy and power densities as well as accelerate the deterioration of reversible capacity and cycle ability due to their electrical insulation and chemical inertness to Li^+.[25,26] Therefore, achieving high-efficient preparation of binder-free integrated anodes for advanced LIBs is obligatory as well.

Herein, freestanding 3D nanoporous Cu supported Cu_2O hierarchical nanoplate arrays were fabricated in-situ by facile one-step electrochemical dealloying of as-cast $Mn_{65}Cu_{35}$ (at.%) alloy slices in the H_2SO_4 solution without removal of oxygen at the potential of 0.2 V (vs. SCE) (named as oxidation-assisted electrochemical dealloying). The as-prepared 3D nanocomposites are characteristic of in-situ growth of Cu_2O HNPAs on uniform 3D nanoporous Cu (NPC) substrate, in which Cu_2O HNPAs are composed of large-sized 2D Cu_2O nanoplate arrays firmly embedded in small-sized counterparts. Compared with other Cu_xO-based electrode materials reported in the literature, the unique 3D nanocomposites as binder-free integrated anodes for LIBs display ultrahigh specific capacity, long cycle life and excellent rate capability, which can deliver a reversible capacity as high as 3.0 mAh cm^{-2} with 71.4% capacity

retention after 450 long-cycles at a current density of 2 mA cm^{-2}. Even if the current density reaches 5 mA cm^{-2}, an ultrahigh reversible capacity of 3.4 mAh cm^{-2} still can be achieved smoothly without obvious capacity decay after 250 cycles. It is totally comparable to or even exceeds the current level of commercial graphite anode, indicating a quite promising anode candicate for advanced LIBs. The formation mechanism of the unique 3D NPC@Cu_2O HNPAs composites and their Li storage properties have been discussed in detail.

II. EXPERIMENTAL

The nominal $Mn_{65}Cu_{35}$ (at.%) alloy ingots were prepared from pure manganese (99.9 wt.%) and pure copper (99.99 wt.%) by vacuum induction furnace. The alloy ingots were cut into slices with thickness of ca. 600 μm by wire cutting machine, and then were ground and mechanically polished to remove oxidation layers on the surfaces. Energy dispersive X-ray (EDX) spectroscopy analysis showed the atomic percentage of Cu and Mn in the as-cast Mn-Cu alloy was quite closely to the designed composition, indicating the alloy slices can be further used in the following study (Table S1). Subsequently, the polished $Mn_{65}Cu_{35}$ alloy slices were electrochemically dealloyed in a 5 wt.% H_2SO_4 solution without removal of oxygen at a constant potential of 0.2V (vs. SCE) at room temperature (RT, ca. 25℃) for different times. The typical dealloying times range from 20 to 80 min. The dealloying process was carried out using an electrochemical workstation (CHI 760E) in a standard three-electrode cell (200 mL) with a Pt plate electrode as a counter electrode, a saturated calomel electrode (SCE) as a reference electrode, and the polished Mn-Cu

alloy slice as a working electrode. Upon the dealloying, the resultant samples were rinsed with distilled water and dehydrated alcohol (analytical grade) for several times, and then dried in a vacuum oven at 70℃ for 24 h. Finally, the 3D NPC@Cu_2O HNPAs composites can be obtained, which were kept in a vacuum chamber to avoid further oxidation before utilization.

Microstructural characterization and analysis of the initial $Mn_{65}Cu_{35}$ (at.%) alloy and as-dealloyed nanocomposites were carried out using X-ray diffraction (XRD, Rigaku D/Max-2400) with Cu K_α radiation (λ=1.5406 Å), scanning electron microscopy (FESEM, Hitachi S-4800) with an EDX analyzer, transmission electron microscopy (TEM, JEOL JEM 2100F) with selected-area electron diffraction (SAED), and high-resolution transmission electron microscopy (HRTEM, JEOL JEM 2100F). The surface chemical composition and valence state of the 3D nanocomposites were examined by X-ray photoelectron spectroscopy (XPS, PHI 5700).

The resultant 3D NPC@Cu_2O HNPAs composites as working electrodes were assembled into coin-type test cells (CR2032) in an Ar-filled glove box (LS-750D, DELLIX) with metal Li foil as both reference and counter electrodes, 1 M $LiPF_6$ in a mixed solution of ethylene carbonate (EC), diethyl carbonate (DEC) and diethyl carbonate (DME) (1:1:1 by v/v/v) as electrolytes, as well as polypropylene (PP) microporous films (Cellgard 2400) as separators. Each half-cell was aged for over 12 h at RT and then starting electrochemical tests. The galvanostatic charge-discharge tests were performed on a multichannel battery test system ((NEWARE BTS-610, Neware Technology Co., Ltd, China) for a cut-off potential

of 0.01-3.0 V (vs. Li/Li^+) under different current densities at ambient temperature (AT). Cyclic voltammograms (CVs) were recorded using a CHI 760E electrochemical workstation between 0.01 to 3.0 V (vs. Li/Li^+) at a scan rate of 0.1 mV s^{-1}. Electrochemical impedance spectroscopy (EIS) measurements were conducted over a frequency range from 0.01 Hz to 1 MHz with AC amplitude of 5 mV. Besides, the Li-ion full cell also were assembled in the Ar-filled glove box by using the 3D NPC@Cu_2O HNPAs electrode without any binder and conductive agent as an anode and $LiCoO_2$ electrode as a cathode, which was fabricated by casting the slurry of $LiCoO_2$ power, PVDF and acetylene black in a mass ratio of 8:1:1 in NMP organic solvent on Al foil and subsequently drying in a vacuum oven at 75℃ for 12 h. Celgard 2400 microporous film was used as a separator and 1 M $LiPF_6$ was dissolved in a mixture of EC, DEC and DMC (1:1:1 by v/v/v) as the electrolyte. The electrochemical performance of the assembled full cells was measured further on the NEWARE multichannel battery test system at a voltage range of 0.8-3.7 V after aging for 24 h at AT.

III. RESULTS AND DISCUSSION

The in-situ preparation flow of freestanding 3D NPC@Cu_2O HNPAs composites by the one-step oxidation-assisted electrochemical dealloying has been schematically illustrated in Figure 1a. Figure 1b-d shows the planar and cross-sectional SEM images of 3D NPC@Cu_2O HNPAs composites by the one-step dealloying of as-cast $Mn_{65}Cu_{35}$ (at.%) alloy slices in the H_2SO_4 solution at 0.2 V (vs. SCE) for 80 min. As can be seen clearly in Figure 2b, a plenty of vertical nanoplate arrays were

interlaced regularly to form relatively uniform flower-like porous structure with a length scale of hundreds of nm. The SEM image in a higher magnification further exhibits that these vertical nanoplates possess smooth surfaces and feature sizes of ca. 800 nm in length and ca. 50 nm in thickness (Figure 2c). Interestingly, note that there are many small-sized nanoplate arrays at the bottom of flower-like porous structure surrounded by the large-sized nanoplates. In order to observe them more clearly, the cross-sectional SEM image is further revealed in Figure 1d. It is obvious that the microstructure of the as-dealloyed products mainly involves three parts from bottom to top: uniform 3D NP substrate with ligament/pore sizes of tens of nm, small-sized interlaced nanoplate arrays with tens of nm in length and several nm in thickness, as well as larged-sized nanoplate arrays with hundreds of nm in length and tens of nm in thickness. Meanwhile, it can be found easily that the large-sized nanoplate arrays are firmly embedded in the small-sized counterparts that in-situ growing on the 3D NP substrate, in which the small-sized nanoplate arrays can serve as intermediate layers to effectively link up the large-sized counterparts with the 3D porous substrate. EDX analysis shows Cu and O elements can be detected simultaneously on the surfaces of the as-dealloyed products and their atomic ratio is quite closely to 2:1, suggesting that these vertical nanoplate arrays are composed of Cu_2O (Figure 1e); in contrast, nearly single Cu element can be determined at the bottom of the as-dealloyed products, indicating that the 3D porous substrate is Cu (Figure S1). Besides, EDX mapping results in Figure 1f-g further reveal the fairly uniform distribution of Cu and O elements on the surfaces of the 3D composites. Figure 1h clearly displays the regional

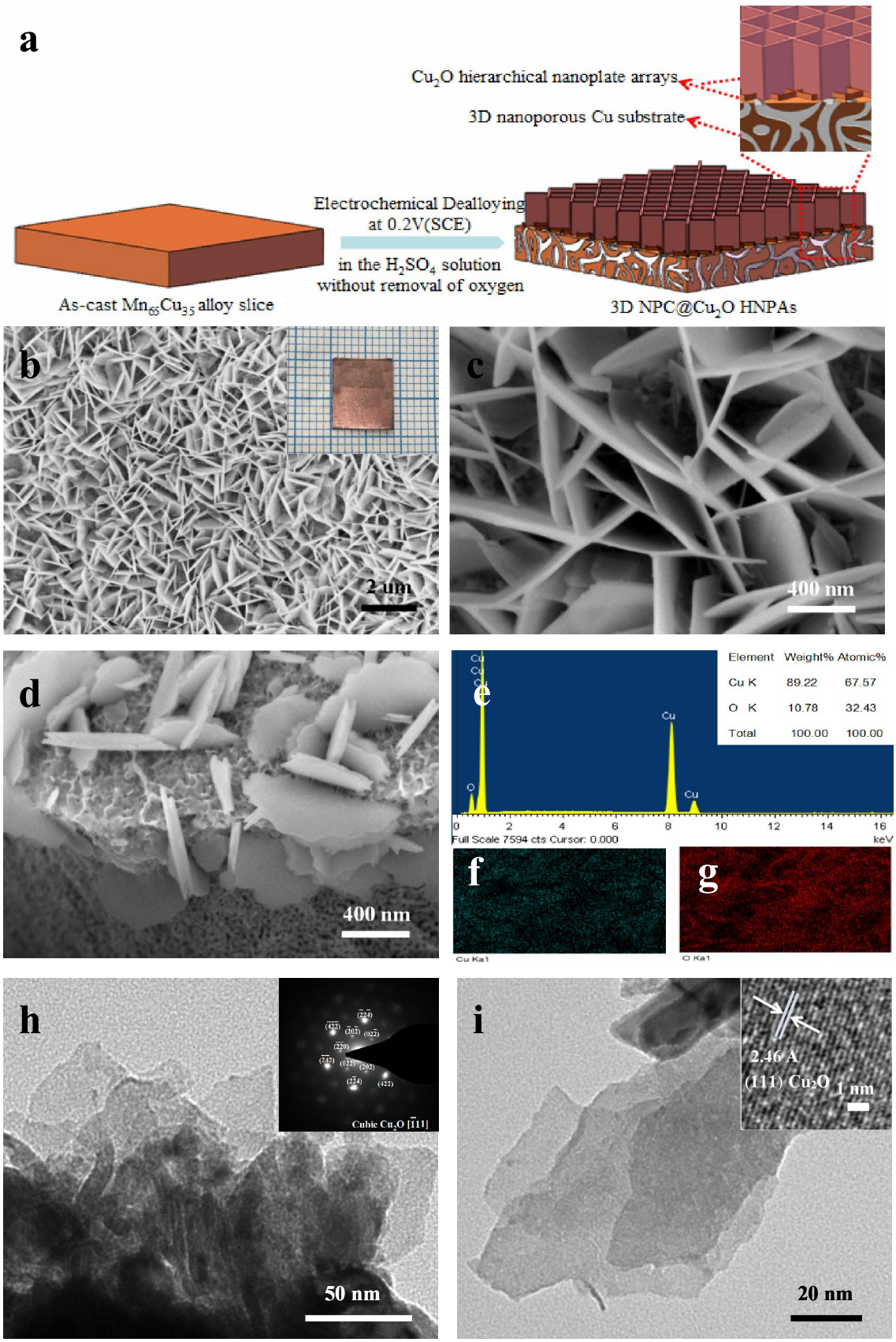

Figure 1. (a) Schematic of preparation process of freestanding 3D NPC@Cu_2O HNPAs composites. (b,c) Planar and (d) cross-sectional SEM images of 3D NPC@Cu_2O HNPAs composites by electrochemical dealloying of as-cast $Mn_{65}Cu_{35}$

(at.%) alloy slices in the H_2SO_4 solution without removal of oxygen at 0.2 V (vs. SCE) for 80 min. The inset in part b is the typical digital picture of 3D NPC@Cu_2O HNPAs composites. (e) EDX spectrum and (f,g) Cu, O mapping results of surface structure of 3D NPC@Cu_2O HNPAs composites. (h and inset) TEM image and SAED pattern of 3D NPC@Cu_2O HNPAs composites. (i and inset) High-magnification TEM and HRTEM images of a typical Cu_2O nanoplate in 3D NPC@Cu_2O HNPAs composites.

TEM image of the 3D NPC@Cu_2O HNPAs composites, in which the small-sized nanoplate arrays in-situ grow on the 3D NP substrate. The SAED pattern corresponding to one nanoplate exhibits an equilateral hexagon pattern, which stems from the cubic Cu_2O $[\bar{1}11]$ zone axis, indicating its typical single crystalline feature (inset of Figure 1h). Moreover, the high-magnification TEM image of a typcial small-sized ultrathin nanoplate is displayed in Figure 1i, in which the lattice fringe with interplanar spacing of 0.246 nm throughout the whole nanoplate in the HRTEM image further certifies its single crystal nature. Thus, we can herein define the unqiue Cu_2O nanoplate arrays with two kinds of feature sizes as Cu_2O HNPAs and the distinct 3D composites with three kinds of typical structures as 3D NPC@Cu_2O HNPAs.

Figure 2a shows the XRD patterns of the initial $Mn_{65}Cu_{35}$ (at.%) alloy and resultant 3D nanocomposites by the one-step dealloying. As can be seen clearly, for the initial Mn-Cu alloy, the diffraction peaks located at $2\theta=41.9°$ and 48.1° correspond well to (101) and (110) planes of tetragonal (Mn, Cu) solid solution (JCPDS No. 04-0823). In contrast, for the 3D composites upon the dealloying, the three strong diffraction peaks situated at $2\theta=43.3°$, 50.4° and 74.1° match with (111), (200) and (220) planes of f.c.c Cu phase (JCPDS No. 48-1548), while other diffraction peaks located at $2\theta=29.5°$,

36.4°, 42° and 61.4° assign to (110), (111), (200) and (220) planes of cubic Cu_2O (JCPDS No. 34-1354), exactly indicative of the co-existence of Cu_2O and Cu in the as-dealloyed products. This is well coincident with the EDX results.

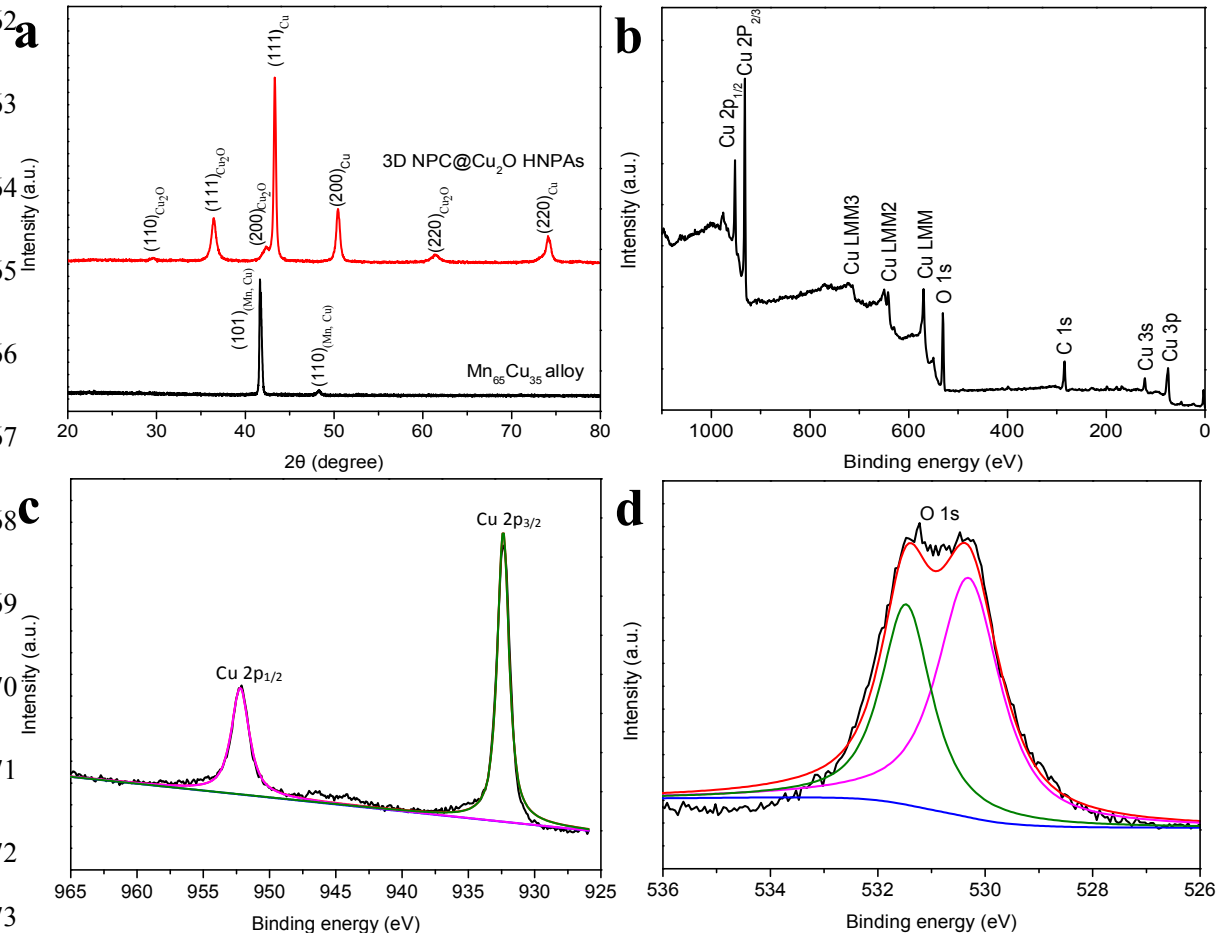

Figure 2. (a) XRD patterns of initial $Mn_{65}Cu_{35}$ alloy and resultant 3D NPC@Cu_2O HNPAs composites by the one-step oxidation-assisted electrochemical dealloying. (b) XPS survey spectra of 3D NPC@Cu_2O HNPAs composites. (c,d) High-resolution XPS spectra of Cu 2p and O 1s for 3D NPC@Cu_2O HNPAs composites.

The surface chemical composition and valence state of the as-synthesized 3D nanocomposites are measured further by XPS, as presented in Figure 2b-d. Obviously, the signal peaks of Cu and O elements can be detected simultaneously on the sample surfaces in a relatively wide range of binding energy (Figure 2b). The high-resolution XPS spectrum of Cu 2p in Figure 2c further displays the two peaks located at 952.2

284 and 932.4 eV, corresponding to the Cu $2p_{1/2}$ peak of Cu(I) as well as the Cu $2p_{3/2}$ peak
285 of Cu(I) and/or Cu(0), respectively.[27] Thus, it is necessary to further investigate the
286 high-resolution O 1s spectrum in order to distinguish Cu(I) from Cu(0), as shown in
287 Figure 2d. Obviously, the high-resolution XPS spectrum of O 1s can be decomposed
288 into two fitting peaks, in which the peak at 530.3 eV corresponds to lattice oxygen
289 within cuprous oxide, while the other peak at 531.4 eV may be from O_2 adsorbed
290 physically on sample surfaces.[28] The present XPS results further confirm that Cu_2O
291 is the single product formed on the sample surfaces during the dealloying, which is in
292 good line with the EDX and XRD analysis above.

293 In order to reveal the formation process during the electrochemical dealloying, the
294 microstructure evolution with dealloying times of 3D NPC@Cu_2O HNPAs
295 composites was investigated further, as depicted in Figure 3. As the dealloying time is
296 just 20 min, the small-sized Cu_2O nanoplate arrays with uniform distribution and
297 interlaced arrangement can be formed well to make up the regular flower-like porous
298 structure in the same scale, while just a few uneven, isolated large-sized counterparts
299 can be observed simultaneously (Figure 3a). Note that the 3D NP substrate has been
300 well-created at this moment, as shown in the inset of Figure 3a. With the gradual
301 increase of dealloying time from 20 to 60 min, the large-sized Cu_2O nanoplate arrays
302 grow more, larger and denser to be interlaced with each other and firmly embedded in
303 the small-sized counterparts (Figure 3b-c); in contrast, the 3D NP substrate has no
304 obvious structure change other than slight coarsening (insets of Figure 3b-c). As the
305 dealloying time reaches 80 min, the uniform large-sized Cu_2O nanoplate arrays

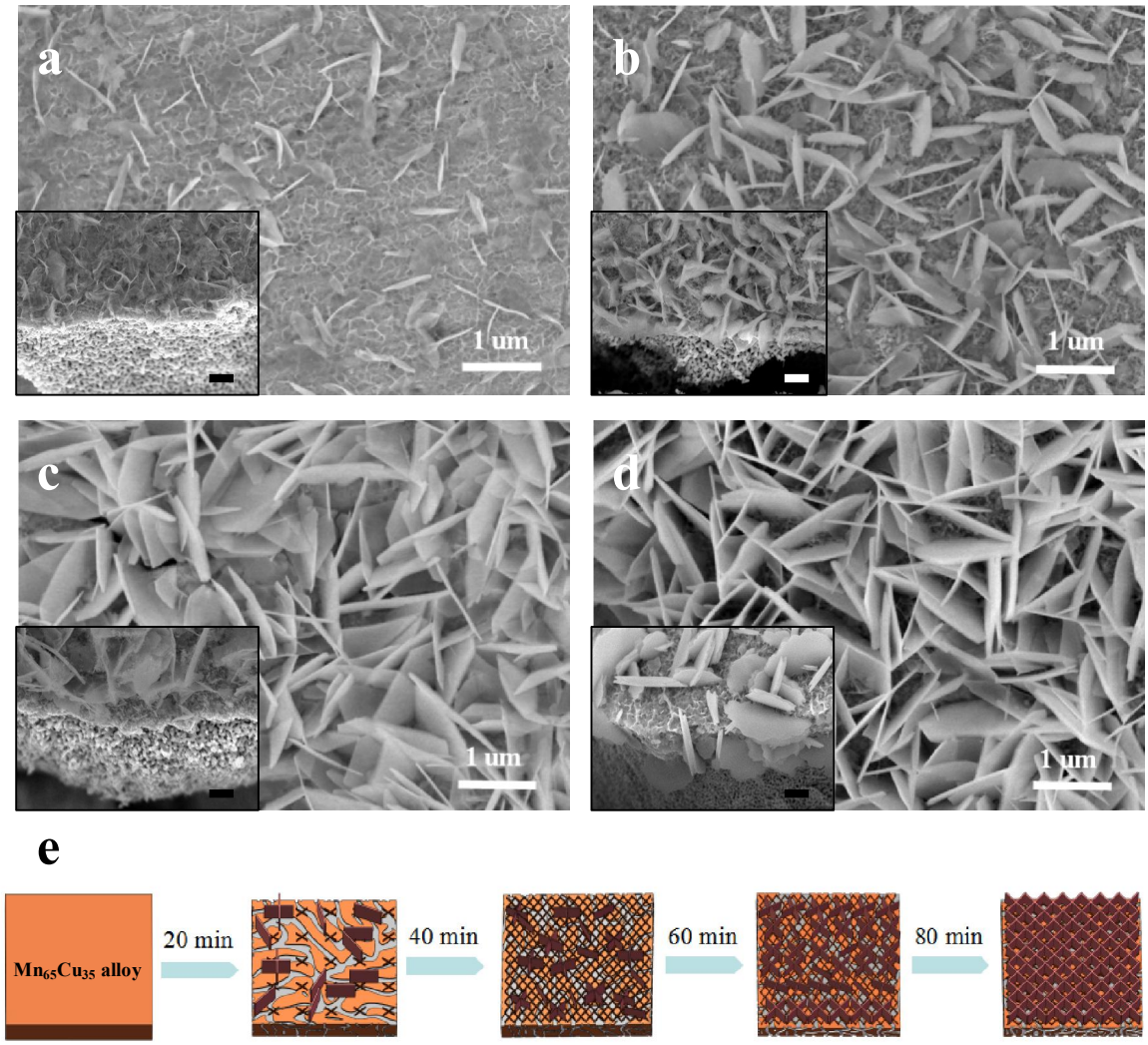

Figure 3. The microstructure evolution of 3D NPC@Cu_2O HNPAs composites during electrochemical dealloying at the potential of 0.2 V (vs. SCE) for (a) 20 min, (b) 40 min, (c) 60 min, and (d) 80 min. The insets in parts a-d are the corresponding cross-sectional SEM images. Scale bar: 250 nm. (e) Schematic illustration of the in-situ formation of 3D NPC@Cu_2O HNPAs composites.

with regular flower-like porous structure can be achieved perfectly on the 3D NP substrate, eventually leading to the in-situ formation of 3D NPC@Cu_2O HNPAs composites (Figure 3d). The schematic of formation process has been systematically summarized in Figure 3e. On the other hand, we also can exploratively elucidate their evolution mechanism at the atomic level. At the beginning of the dealloying, the Mn atoms in the initial Mn-Cu alloy continuously dissolve into the solution and the

remaining Cu will reassemble to form the 3D NP structure by rapid surface diffusion along the alloy/solution interfaces, which has been well-demonstrated in the previous literature;[29,30] meanwhile, the dissolved active oxygen radical (•O) in the H_2SO_4 solution can be arrested fast by activated Cu atoms on the 3D NP surfaces with unsaturated bond and high surface energy to generate a large number of small-sized and a small number of large-sized Cu_2O nanoplate arrays under the effect of applied electric field. With the dealloying time continually increasing, more small-sized Cu_2O nanoplates with suitable orientation will grow up preferentially to become the large-sized counterparts, while the escalation of large-sized Cu_2O nanoplates in turn inhibits the preferred orientation and subsequent growth of small-sized counterparts, finally resulting in the in-situ formation of Cu_2O HNPAs on the 3D NP substrate. This is in good accordance with the SEM observations described above.

To verify its superiority as a binder-free integrated anode for LIBs, the Li storage properties of 3D NPC@Cu_2O HNPAs composites were investigated systematically; meanwhile, for clear comparison, the 2D copper foil supported Cu_2O microparticles (2D CF@Cu_2O MPs) also were prepared by simple two-step thermal treatments of 2D CF in air at 550℃ for 1 h and then in Ar at 700℃ for 2 h (see the Supplementary Material for detailed preparation process and related SEM, EDX, XRD results, Figure S2). Figure 4a shows the initial three-cycle CVs of 3D NPC@Cu_2O HNPAs electrode between 0.01 and 3.0 V (vs. Li/Li^+) at a scan rate of 0.1 mV s^{-1}. Obviously, just a broad cathodic peak can be found easily at 0.87 V (vs. Li/Li^+) in the first negative scan, which essentially corresponds to the overlap of two cathodic peaks involving

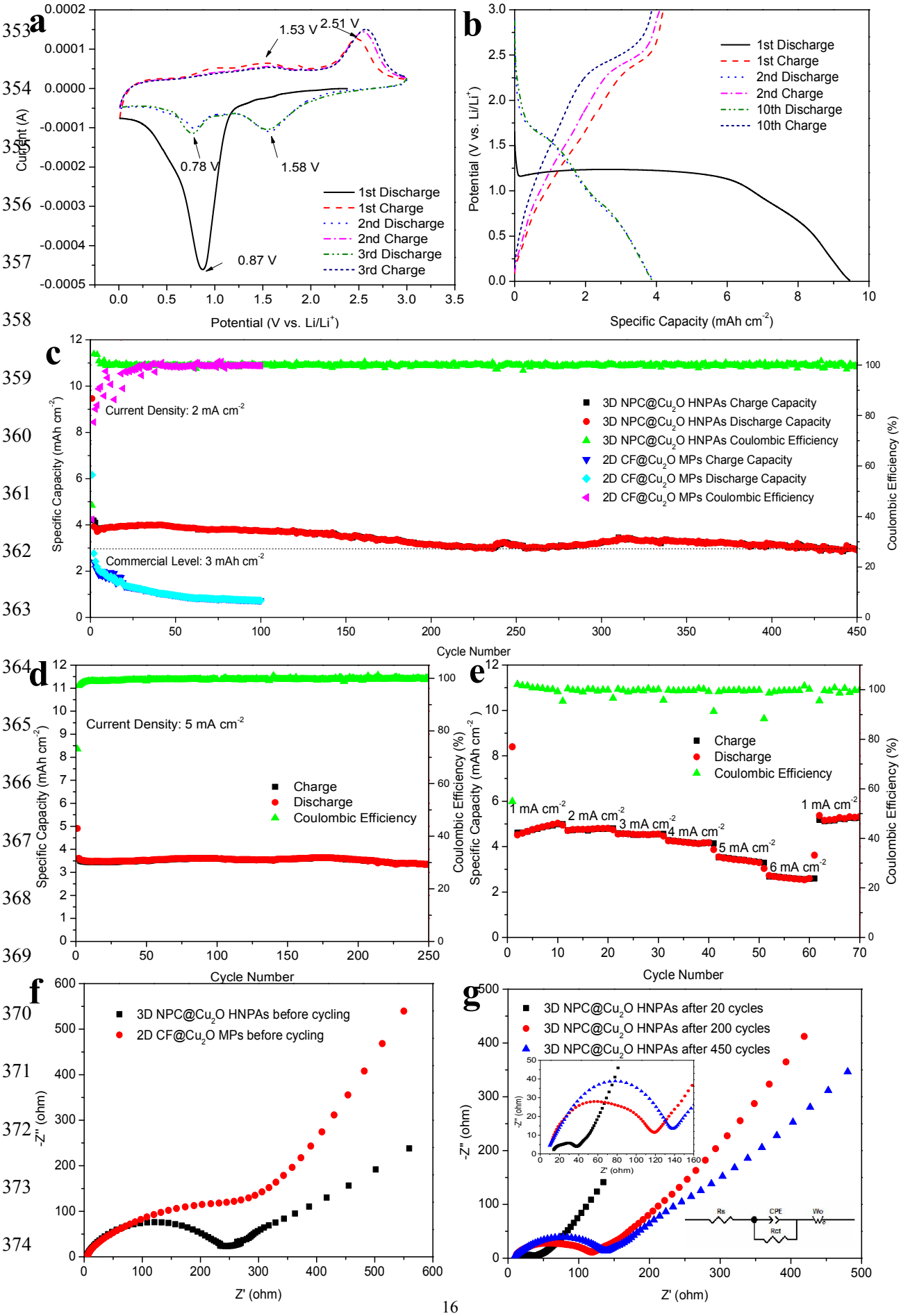
a
1.53 V
2.51 V
0.78 V
1.58 V
0.87 V
1st Discharge
1st Charge
2nd Discharge
2nd Charge
3rd Discharge
3rd Charge
Current (A)
Potential (V vs. Li/Li+)
b
1st Discharge
1st Charge
2nd Discharge
2nd Charge
10th Discharge
10th Charge
Potential (V vs. Li/Li+)
Specific Capacity (mAh cm-2)
c
Current Density: 2 mA cm-2
Commercial Level: 3 mAh cm-2
3D NPC@Cu2O HNPAs Charge Capacity
3D NPC@Cu2O HNPAs Discharge Capacity
3D NPC@Cu2O HNPAs Coulombic Efficiency
2D CF@Cu2O MPs Charge Capacity
2D CF@Cu2O MPs Discharge Capacity
2D CF@Cu2O MPs Coulombic Efficiency
Specific Capacity (mAh cm-2)
Coulombic Efficiency (%)
Cycle Number
d
Current Density: 5 mA cm-2
Charge
Discharge
Coulombic Efficiency
Specific Capacity (mAh cm-2)
Coulombic Efficiency (%)
Cycle Number
e
Charge
Discharge
Coulombic Efficiency
1 mA cm-2
2 mA cm-2
3 mA cm-2
4 mA cm-2
5 mA cm-2
6 mA cm-2
1 mA cm-2
Specific Capacity (mAh cm-2)
Coulombic Efficiency (%)
Cycle Number
f
3D NPC@Cu2O HNPAs before cycling
2D CF@Cu2O MPs before cycling
-Z'' (ohm)
Z' (ohm)
g
3D NPC@Cu2O HNPAs after 20 cycles
3D NPC@Cu2O HNPAs after 200 cycles
3D NPC@Cu2O HNPAs after 450 cycles
-Z'' (ohm)
Z' (ohm)
Rs
CPE
Wo
Rct

Figure 4. (a) CVs of 3D NPC@Cu_2O HNPAs electrode ranging from 0.01 to 3.0 V (vs. Li/Li^+) at a scan rate of 0.1 mV s^{-1}. (b) Potential vs. capacity plots of 3D NPC@Cu_2O HNPAs electrode at a current density of 2 mA cm^{-2}. (c) Cycle performance of 3D NPC@Cu_2O HNPAs and 2D CF@Cu_2O MPs electrodes at a current density of 2 mA cm^{-2}. (d) Galvanostatic charge-discharge curves of 3D NPC@Cu_2O HNPAs electrode at an elevated current density of 5 mA cm^{-2}. (e) Rate capability profiles of 3D NPC@Cu_2O HNPAs electrode at different current densities. Nyquist plots of (f) 3D NPC@Cu_2O HNPAs and 2D CF@Cu_2O MPs electrodes before cycling, and (g) 3D NPC@Cu_2O HNPAs electrode after 20, 200 and 450 charge-discharge cycles. Insets in part g are the locally amplified high-frequency zone and equivalent circuit of EIS of 3D NPC@Cu_2O HNPAs electrode after cycling.

reduction of Cu_2O to Cu ($Cu_2O + 2Li^+ + 2e^- \rightarrow 2Cu + Li_2O$) and formation of solid electrolyte interface (SEI) films between Cu_2O and electrolyte, respectively.[31-33] In contrast, in the first positive scan, there are two apparent anodic peaks located at 1.53 and 2.51 V (vs. Li/Li^+), which can be ascribed well to the decomposition of SEI films and reverse conversion of Cu to Cu_2O ($2Cu + Li_2O \rightarrow 2Li^+ + 2e^- + Cu_2O$).[7] It should be noted, however, that in the second negative scan, the initial board reduction peak at 0.87 V (vs. Li/Li^+) disappears and instead two new reduction peaks at 1.58 and 0.78 V (vs. Li/Li^+) emerge, designating to the reduction of Cu_2O and formation of SEI films, respectively. Compared to the first negative scan, the obvious positive shift of reduction potential of Cu_2O in the second scan is closely related to the significant decrease in feature size of Cu_2O from micron to nanometre after the initial lithiation reaction.[34-36] In addition, the 2nd and 3rd CVs are well overlapped with each other, indicating its excellent cycling stability and electrochemical reversibility.

Figure 4b displays the potential vs. capacity profiles of 3D NPC@Cu_2O HNPAs electrode with a cut-off potential of 0.01-3.0 V (vs. Li/Li^+) at a current density of 2 mA cm^{-2}. As can be seen clearly, the 1st discharge and charge processes delivered the

403 ultrahigh specific capacities of 9.2 and 4.2 mAh cm^{-2}, respectively, with ca. 46%
404 coulombic efficiency. The initial capacity loss mainly stems from the partial
405 irreversible conversion of Cu_2O, formation of SEI films and interfacial spaces
406 consuming lots of Li^+.[37] In fact, this phenomenon can be found in most
407 TMOs-based electrode materials.[5,38] The 2nd and 10th charge processes delivered
408 the reversible specific capacities as high as 4.1 and 3.9 mAh cm^{-2} with 97.6% and
409 92.9% capacity retentions respectively, suggesting its favorable structure stability
410 during repetitive lithiation-delithiation processes. Note that the difference between
411 charge and discharge capacities is only 0.09 and 0.01 mAh cm^{-2} for the 2nd and 10th
412 cycles, as well as the 10th charge-discharge profile can overlap well with the 2nd one,
413 fully demonstrating its excellent electrochemical reversibility. Additionally, the 1st
414 discharge plateau from 1.2 to 0.8 V (vs. Li/Li^+) can be replaced completely by two
415 new counterparts from 1.75 to 1.5 V (vs. Li/Li^+) and 1.0 to 0.75 V (vs. Li/Li^+) in the
416 subsequent cycles, which is in good agreement with the CVs in Figure 4a.

417 Figure 4c displays the cycle performance of 3D NPC@Cu_2O HNPAs electrode at a
418 current density of 2 mA cm^{-2}; meanwhile, the counterpart of 2D CF@Cu_2O MPs
419 electrode also is tested under the same conditions. Compared to the 2D electrode, the
420 3D NPC@Cu_2O HNPAs electrode shows the notably higher specific capacity, longer
421 cycle life and more steady coulombic efficiency, indicating that the unique 3D
422 electrode architecture plays a critical role in increasing the active material loadings,
423 alleviating the large volume change and improving the structural stability. Specifically,
424 after a quite slight capacity decrease in the initial several cycles, the 3D NPC@Cu_2O

425 HNPAs electrode retains superior cycling ability with reversible capacity retentions of
426 ca. 88.1% after 100 cycles and over 71.4% after elongated 450 cycles. Except for the
427 first several cycles, its coulombic efficiency is always beyond 99.6%, indicative of
428 outstanding electrochemical reversibility. Typically, the reversible specific capacities
429 of 3.91, 3.73 and 3.51 mAh cm^{-2} can be reached at the 50th, 100th and 150th cycles
430 for the 3D electrode, respectively. Even if after 450 long-cycles, it still can deliver an
431 ultrahigh reversible capacity of 3.0 mAh cm^{-2} steadily, which is totally comparable to
432 or even exceeds the current level of commercial graphite anode. In contrast, the
433 reversible capacities of 1.77, 0.95 and 0.73 mAh cm^{-2} can be obtained for the 2D
434 electrode at the 10th, 50th and 100th cycles respectively, which is just one fifth less
435 than the 3D electrode after 100 cycles. Particularly, the reversible capacity of the 2D
436 electrode drastically decreases from the beginning and only 30.5% capacity retention
437 remains at the 100th cycle. The poor capacity retention is mainly related to the 2D
438 planar substrate structure and compact stacking of active material in micron scale,
439 which would result in the inadequate buffering of mechanical strain caused by large
440 volume variation during repeated lithiation-delithiation processes as well as the rapid
441 exfoliation of active material from the 2D planar substrate surface. To further confirm
442 the superiority of 3D NPC@Cu_2O HNPAs electrode, the galvanostatic
443 charge-discharge curve was recorded at an elevated current density of 5 mA cm^{-2}, as
444 shown in Figure 4d. It is exciting that the reversible capacity as high as 3.4 mAh cm^{-2}
445 can be obtained smoothly without obvious capacity decay after 250 cycles, indicating
446 its superior cycling stability. Additionally, the Li storage property of 3D NPC@Cu_2O

447 HNPAs electrode was systematically compared with other Cu_xO-based composite
448 electrodes with different nanostructure designs reported in the recent literature, as
449 listed in detail in Table S2. Evidently, the better cycling stability and longer cycle life
450 can be achieved well in the 3D NPC@Cu_2O HNPAs electrode.

451 The rate capability of 3D NPC@Cu_2O HNPAs electrode was tested further under
452 different current densities, as presented in Figure 4e, which is another key assessment
453 for electrochemical properties of LIBs. Clearly, the discharge and charge capacities
454 gradually decrease with the continual increase of current density, which is closely
455 associated with the increasing electrode polarization; however, note that the capacity
456 difference between adjacent current densities is always very small and the reversible
457 capacity can promptly recover as the current density gets back to the initial value
458 again, implying its excellent structure stability and rate performance. Typically, the
459 large reversible capacities of 5.0, 4.8, 4.5, 4.1, 3.3 and 2.6 mAh cm^{-2} can be attained
460 after each 10 cycles at the current densities of 1, 2, 3, 4, 5 and 6 mA cm^{-2}, respectively.
461 When the current density returns to 1 mA cm^{-2} again, the reversible capacity quickly
462 rises to 5.17 mAh cm^{-2}, maintaining as high as ca. 103% capacity retention relative to
463 that of the 10th cycle at the same current density, which is likely owing to the
464 fractional decomposition of SEI films and organic electrolyte.[39-42] Note that after
465 experiencing a series of high-rate charge-discharge processes, the reversible specific
466 capacity still can reach 5.2 mAh cm^{-2} after 70 cycles, suggesting its superior rate
467 capability. This can be largely attributed to the unique 3D electrode architecture
468 comprising HNPAs and NP substrate, which can not only accelerate the electrolyte

permeation, but provide the fast Li^+/electron transfer channels at electrode/electrolyte and current collector/active material interfaces. In addition, the small-sized Cu_2O nanoplate arrays can act as intermediate layers to closely connect the large-sized nanoplate arrays with lots of electrochemical active sites to the 3D NP substrate with good electrical conductivity, thus enhancing the binding force between active material and substrate as well as improving the structure integrity of electrode markedly.

To further reveal the Li^+ and electron transfer kinetics, the Nyquist plots of 3D NPC@Cu_2O HNPAs and 2D CF@Cu_2O MPs electrodes before and after cycling were investigated by EIS, as depicted in Figure 4f-g. It is obvious that all Nyquist plots consist of a compressed semicircle in high-medium frequency area, the diameter of which stands for charge transfer resistance (R_{ct}) related to electrochemical reactions on electrode/electrolyte interfaces, and an oblique line in low frequency area closely associated with Li^+ diffusion coefficient in electrode materials.[27,43-45] As indicated in Figure 4f, the 3D electrode before cycling has a significantly low R_{ct} (ca. 280 Ω) compared to that of the 2D electrode (ca. 600 Ω), implying its better conductivity. Note that the R_{ct} of the 3D electrode reduces fiercely after 20 cycles (ca. 40 Ω); even after 200 and 450 cycles, the R_{ct} values still can be determined to be just ca. 120 and 140 Ω, slightly greater than that after 20 cycles but far lower than those of the original 2D and 3D electrodes, fully demonstrating the excellent Li^+/electron transfer abilities of the 3D electrode during cycling. To understand this issue from a quantitative perspective, the equivalent circuit of EIS of 3D NPC@Cu_2O HNPAs electrode has been fitted further, as depicted in the inset of Figure 4g. It is mainly composed of

related circuit models including electrolyte resistance R_s, charge transfer resistance R_{ct}, Warburg impedance of Li^+ diffusion in electrode W_o, and space charge capacitance at electrode/electrolyte interface CPE. Clearly, the R_s and R_{ct} values of the 3D electrode can be identified to be ca. 9.6 and 36.2 Ω after 20 cycles, 5.4 and 113.5 Ω after 200 cycles, as well as 8.6 and 138.1 Ω after 450 cycles, respectively. The present results manifest that the unique 3D electrode architecture design (uniform 3D NP substrate, Cu_2O HNPAs and good binding force between them by in-situ growth and compact joint of intermediate nanolayer) greatly facilitates to shorten the Li^+ diffusion distance, enhance the electron transfer ability and improve the electrode/electrolyte wettability.

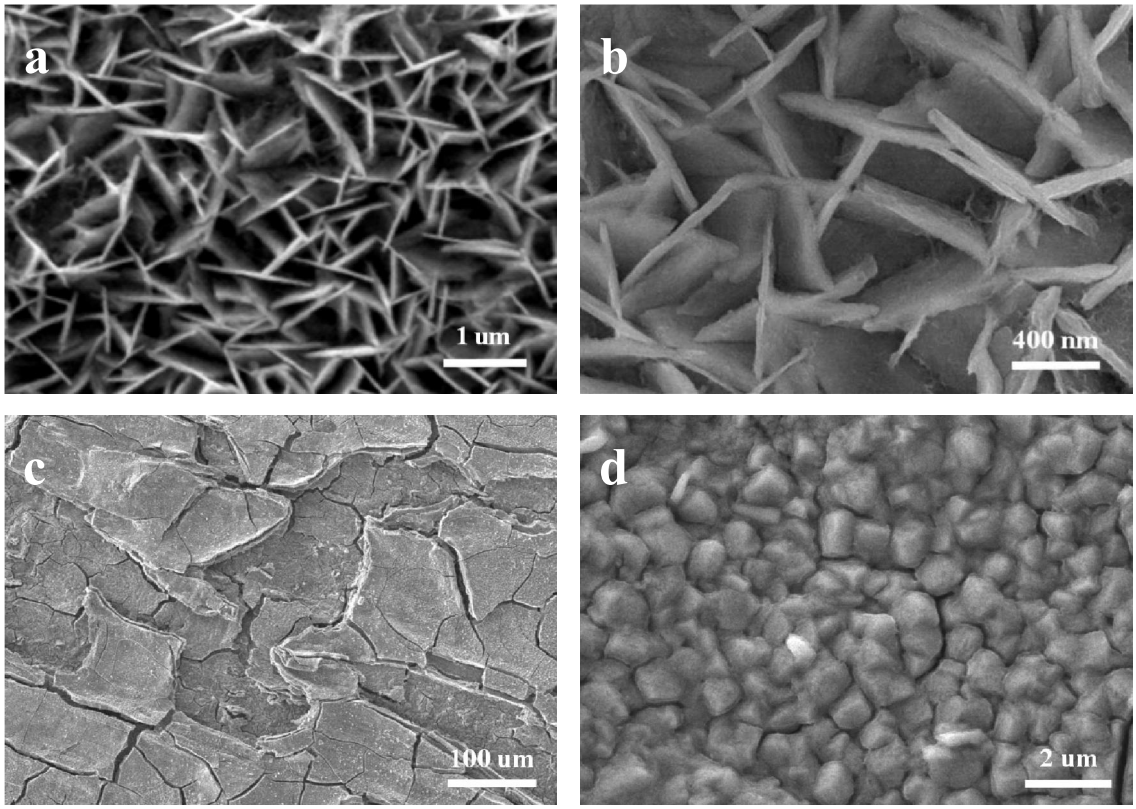

Figure 5. SEM images of (a,b) 3D NPC@Cu_2O HNPAs electrode after 450 long-cycles and (c,d) 2D CF@Cu_2O MPs electrode after 100 cycles at the current density of 2 mA cm^{-2}.

Figure 5a-b shows the microstructure and surface morphology of 3D NPC@Cu_2O

515 HNPAs electrode after cycling at the current density of 2 mA cm^{-2}. It is clear that the
516 nearly perfect Cu_2O HNPAs still can be observed after 450 charge-discharge cycles as
517 well as no obvious cracking, pulverization and exfoliation of Cu_2O nanoplates take
518 place on the electrode surfaces. It indicates that the unique 3D electrode has favorable
519 structural stability and strong adhesive strength, thus buffering mechanical strain and
520 volume variation effectively during repeated lithiation-delithiation processes. Note
521 that the height of flower-like porous structure formed by large-sized Cu_2O nanoplates
522 after cycling appears to be shortened relative to the pristine one, which probably roots
523 in the residual organic electrolyte and bi-products related to SEI formation at the
524 bottom of porous structure.[46] Moreover, the high-magnification SEM image further
525 exhibits the slight coarsening of Cu_2O nanoplates and partial shutdown of porous
526 window due to the accumulated incomplete delithiation during cycling, which would
527 impede the electrolyte penetration and further reaction with internal active material,
528 thus leading to the gradual loss of reversible capacity during elongated cycling
529 (Figure 5b). In contrast, the surface morphology of 2D CF@Cu_2O MPs electrode after
530 cycling was also characterized, as displayed in Figure 5c-d. Obviously, the 2D planar
531 electrode was subjected to severe structure damage with large-scale cracking,
532 pulverization and detachment of Cu_2O MPs from the 2D electrode surfaces just after
533 100 cycles (Figure 5c), which is closely related to the huge volume change and
534 insufficient cushion of mechanical strain during repetitive lithiation-delithiation
535 processes. It is worthwile noting that the SEM image in a higher magnification
536 (Figure 5d) further uncovers the extensive microcracking and serious agglomeration

537 in the surviving Cu_2O MPs after cycling, confirming that the 2D planar electrode
538 cannot effectively accommodate the huge volume change and maintain the structure
539 stability during continuous electrochemical reactions, thus giving rise to the
540 unsatisfactory Li storage performance.

541 Herein, the 3D NPC@Cu_2O HNPAs//$LiCoO_2$ Li-ion full cell was also assembled
542 by using the 3D composite as an anode and commercial $LiCoO_2$ as a cathode to
543 further verify its superiority for potential application in LIBs. As indicated in Figure
544 6a, the voltage vs. capacity profiles of 3D NPC@Cu_2O HNPAs//$LiCoO_2$ full cell
545 were measured in a voltage range of 0.8-3.7 V at a current density of 1 mA cm^{-2}.
546 Clearly, the initial three-cycle discharge processes (Li^+ transfer from 3D NPC@Cu_2O
547 HNPAs to $LiCoO_2$) delivers the high reversible capacities of 2.49, 2.54 and 2.56 mAh
548 cm^{-2}, respectively. Note that the slight capacity increase is mainly owing to the
549 activation of 3D electrode via continual permeation of organic electrolyte at the initial
550 stage of cycling. Moreover, the 1st coulombic efficiency reaches as high as 83.83%,
551 as well as the charge-discharge profiles of 2nd and 3rd cycles overlap well with each
552 other, implying the excellent electrochemical reversibility. Figure 6b shows the cycle
553 performance of 3D NPC@Cu_2O HNPAs//$LiCoO_2$ full cell at a current density of 1
554 mA cm^{-2}. Analogously, the phenomenon on slight increase of discharge capacity also
555 can be observed in the initial several cycles. After that, the Li-ion full cell exhibits the
556 good cycling stability and long cycle life with 80.3% capacity retention after 50
557 cycles, indicating its superior cycling ability. Excitingly, a relatively high reversible
558 capacity of 1.78 mAh cm^{-2} still can be reached smoothly after 100 cycles, which

retains as high as 71.5% capacity retention. Typically, a digital picture of a group of light-emitting diodes (LEDs) lit by the assembled Li-ion full cell with full-charged state after 100 cycles was exhibited in the inset of Figure 6b, further manifesting the good availability of 3D NPC@Cu_2O HNPAs anode toward advanced LIBs.

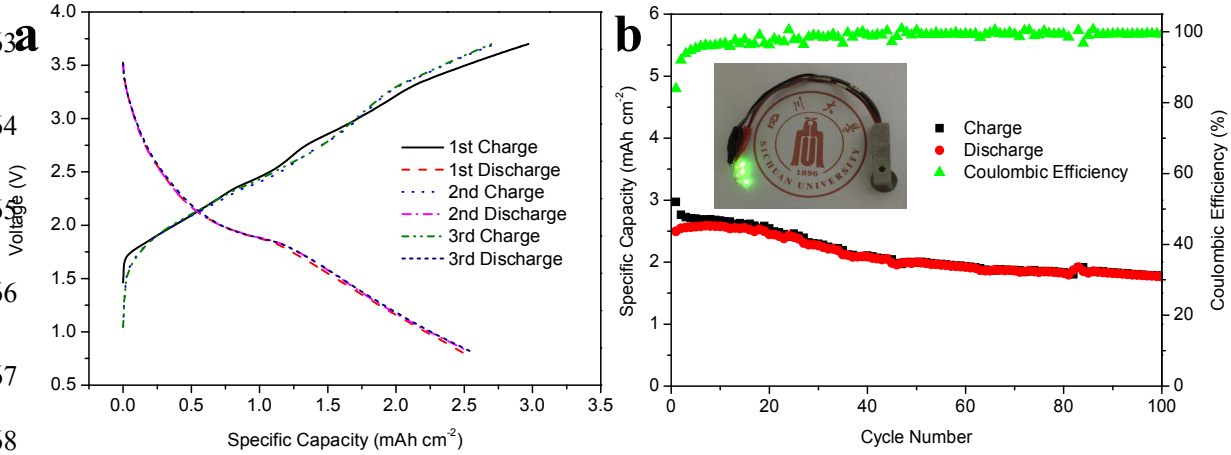

Figure 6. (a) Voltage vs. capacity profiles of 3D NPC@Cu_2O HNPAs//$LiCoO_2$ full cell at a current density of 1 mA cm^{-2}; (b) Cycle performance curves of 3D NPC@Cu_2O HNPAs//$LiCoO_2$ full cell at a current density of 1 mA cm^{-2}, in which the inset presents a digital picture of a group of LEDs lit by the assembled full cell with full-charged state after 100 cycles.

Compared to 2D CF@Cu_2O MPs electrode, the superb electrochemical properties of as-prepared 3D NPC@Cu_2O HNPAs electrode by the one-step dealloying strategy demonstrate the intrinsic advantages of in-situ growth of Cu_2O HNPAs upon 3D NP substrate, as illustrated in Figure 7, which can be explained in detail as follows. (1) The Cu_2O HNPAs with large specific surface areas not only can provide more electrochemical active sites reacting with Li^+ in organic electrolyte, but also cause smaller mechanical strain related to volume expansion and contraction during lithiation-delithiation reactions. (2) The unique 3D electrode configuration comprising HNPAs and NP substrate facilitates the rapid permeation of electrolyte, shortening of

584 Li^+ diffusion distance between electrode and electrolyte, and optimization of electron
585 transfer pathways. (3) The abundant space designed among vertical Cu_2O nanoplates
586 can effectively buffer huge volume and structure changes during charge-discharge
587 processes, maintaining good structure stability. (4) The good binding force between
588 Cu_2O HNPAs and NPC substrate by in-situ growth and intermediate layer joint can
589 markedly prevent Cu_2O nanoplates from cracking, pulverization and rapid exfoliation,
590 realizing good structure integrity. (5) The nonuse of any binders and conductive
591 agents may further ameliorate energy and power densities as it is assembled into LIBs.
592 Besides, the developed in-situ oxidation-assisted electrochemical dealloying strategy
593 also has the characteristics of simple process, low cost and less energy consumption,
594 which could be promoted conveniently within the industry. Therefore, we believe that
595 this present work offers a considerably promising binder-free TMOs-based integrated
596 anode candidate towards practical application of advanced LIBs.

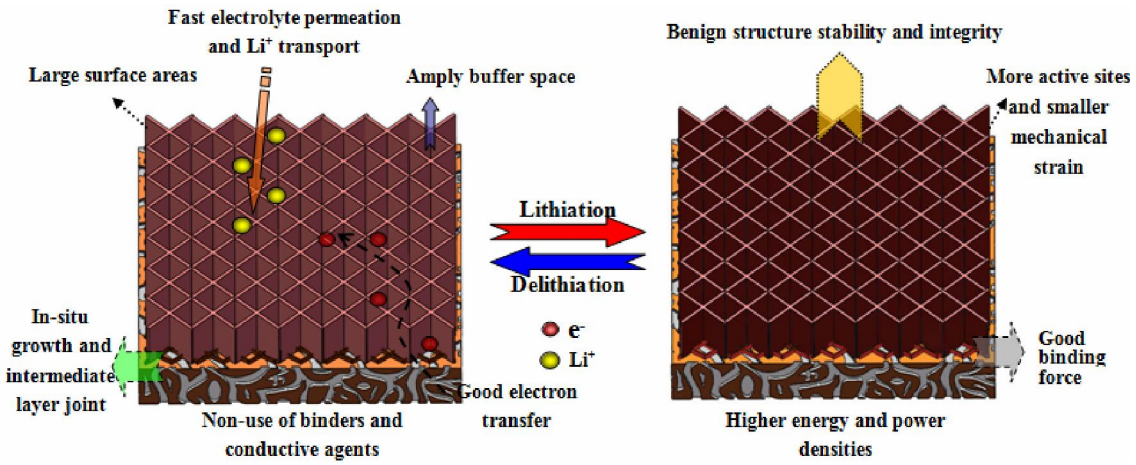

597

598 **Figure 7.** Schematic illustration of lithiation-delithiation processes of 3D NPC@Cu_2O
599 HNPAs electrode.

600

601 **IV. CONCLUSIONS**

In summary, we developed a facile and effective one-step strategy to synthesize the freestanding 3D NPC@Cu_2O HNPAs composites through electrochemical dealloying of as-cast $Mn_{65}Cu_{35}$ (at.%) alloy in the H_2SO_4 solution without removal of oxygen. The as-made 3D nanocomposites are typical of in-situ growth of Cu_2O HNPAs on uniform 3D NPC substrate, in which Cu_2O HNPAs consist of large-sized 2D Cu_2O nanoplate arrays firmly embedded in small-sized counterparts. Compared to other Cu_xO-based electrode materials reported in the literature, the unique 3D nanocomposites as binder-free integrated anodes for LIBs exhibit significantly boosted Li storage performance with ultrahigh initial reversible capacity of 4.2 mAh cm^{-2} and 71.4% capacity retention after 450 cycles at 2 mA cm^{-2}. Even if the current density reaches 5 mA cm^{-2}, an ultrahigh reversible capacity of 3.4 mAh cm^{-2} still can be achieved smoothly without obvious capacity decay after 250 cycles. This can be mainly attributed to the unique 3D electrode structure comprising HNPAs and NP substrate, large contact area between active material and electrolyte, in-situ growth of active material upon porous substrate, compact joint of small-sized intermediate layers, and good mass transfer among vertical hierarchical nanoplates, which can effectively buffer huge volume and structure variations during charge-discharge processes, provide more electrochemical active sites for lithiation/delithiation reactions, enhance binding force between active material and substrate, shorten Li^+ diffusion distance and improve electrical conductivity. Based on their excellent Li storage properties, easy preparation and low cost, we believe that this present work provides a brand-new and high-efficiency route to construct promising TMOs-based

nanostructured anode candidates toward practical application of advanced LIBs.

ACKNOWLEDGMENTS

We give thanks to financial support by the National Natural Science Foundation of China (51604177), the State Key Basic Research Program of PRC (2013CB934001), the Research Grants Council of the Hong Kong Special Administrative Region, China (GRF PolyU152174/17E), the Hong Kong Scholars Program (XJ2014045, G-YZ67), the China Postdoctoral Science Foundation (2015M570784), the Chengdu International S&T Cooperation Funded Project (2019-GH02-00015-HZ), the "1000 Talents Plan" of Sichuan Province, the Fundamental Research Funds for the Central Universities, and the Talent Introduction Program of Sichuan University (YJ201410). Additionally, the authors specially thank Dr. Jiazhen Yan and Long Chen (Sichuan University) for useful discussions and thank Dr Shanling Wang (Analytical & Testing Center, Sichuan University) for help in characterizing (HR)TEM.

CONFLICT OF INTEREST

The authors declare no conflict of interest.

ELECTRONIC SUPPLEMENTARY MATERIAL

The online version of this article (https://) contains supplementary material, which is available to authorized users.

REFERENCES

1. M. Armand and J.M. Tarascon: *Nature*, 2008, vol. 451, pp. 652-57.

2. V. Etacheri, R. Marom, R. Elazari, G. Salitra, and D. Aurbach: *Energy Environ. Sci.*, 2011, vol. 4, pp. 3243-62.

3. D.J. Xue, J. Tan, J.S. Hu, W. Hu, Y.G. Guo, and L.J. Wan: *Adv. Mater.*, 2012, vol. 24, pp. 4528-33.

4. Q.B. Zhang, H.X. Chen, L.L. Luo, B.T. Zhao, H. Luo, X. Han, J.W. Wang, C.M. Wang, Y. Yang, T. Zhu, and M.L. Liu: *Energy Environ. Sci.,* 2018, vol. 11, pp. 669-81.

5. P. Liang, H. Zhang, Y. Su, Z. Huang, C.A. Wang, and M. Zhong: *J. Mater. Chem. A,* 2017, vol. 5, pp. 19781-89.

6. X. Dong, W.B. Liu, X. Chen, J.Z. Yan, N. Li, S.Q. Shi, S.C. Zhang, and X. S. Yang: *Chem. Eng. J.*, 2018, vol. 350, pp. 791-98.

7. P. Poizot, S. Laruelle, S. Grugeon, L. Dupont, and J.M. Tarascon: *Nature,* 2000, vol. 407, pp. 496-99.

8. X. Chen, N.Q. Zhang, and K.N. Sun: *J. Mater. Chem.,* 2012, vol. 22, pp. 15080-84.

9. X.Y. Shen, S. Chen, D.B. Mu, B.R. Wu, and F. Wu: *J. Power Sources,* 2013, vol. 238, pp. 173-79.

10. Y.H. Lee, I.C. Leu, C.L. Liao, S.T. Chang, M.T. Wu, J.H. Yen, and K.Z. Fung: *Electrochem. Solid-State Lett.,* 2006, vol. 9, pp. A207-10.

11. M. Hasan, T. Chowdhury, and J.F. Rohan: *J. Electrochem. Soc.*, 2010, vol. 157, pp. A682-88.

12. W.B. Liu, L. Chen, L. Cui, J.Z. Yan, S.C. Zhang, and S.Q. Shi: *J. Mater. Chem. A*, 2019, vol. 7, pp. 15089-100.

13. Z. Deng, Y.H. Li, Z.Y. Ma, J. Zhao, J.Y. Cao, and D. Zhang: *Curr. Nanosci.*, 2015, vol. 11, pp. 470-74.

14. S.H. Wu, G.L. Fu, W.Q. Lv, J.K. Wei, W.J. Chen, H.Q. Yi, M. Gu, X.D. Bai, L. Zhu, C. Tan, Y.C. Liang, G.L. Zhu, J.R. He, X.Q. Wang, H.L. Zhang, J. Xiong, and W.D. He: *Small,* 2018, vol. 14, pp. 1702667.

15. J.H. Shin, S.H. Park, S.M. Hyun, J.W. Kim, H.M. Park, and J.Y. Song: *Phys. Chem. Chem. Phys.,* 2014, vol. 16, pp. 18226-32.

16. D. Ji, H. Zhou, Y.L. Tong, J.P. Wang, M.Z. Zhu, T.H. Chen, and A.H. Yuan: *Chem. Eng. J.,* 2017, vol. 313, pp. 1623-32.

17. H.P. Zhao, M. Zhou, L.Y. Wen, and Y. Lei: *Nano Energy*, 2015, vol. 13, pp. 790-813.

18. L. Taberna, S. Mitra, P. Poizot, P. Simon, and J.M. Tarascon: *Nat. Mater*., 2006, vol. 5, pp. 567-73.

19. J. Qu, H.Q. Li, J.J. Henry, S.K. Martha, N.J. Dudney, H.B. Xu, M.F. Chi, M.J. Lance, S.M. Mahurin, T.M. Besmann, and S. Dai: *J. Power Sources,* 2012, vol. 198, pp. 312-17.

20. J. Hassoun, S. Panero, P. Simon, P.L. Taberna, and B. Scrosati: *Adv. Mater*., 2007, vol. 19, pp. 1632-35.

21. J.Z. Wang, N. Du, Z.Q. Song, H. Wu, H. Zhang, and D.R. Yang: *RCS Adv.,* 2013, vol. 3, pp. 7543-48.

22. W.B. Liu, S.C. Zhang, N. Li, J.W. Zheng, and Y.L. Xing: *Micropor. Mesopor. Mat.*, 2011, vol. 138, pp. 1-7.

23. W.B. Liu, S.C. Zhang, N. Li, J.W. Zheng, S.S. An, and Y.L. Xing: *Int. J. Electrochem. Sci*., 2011, vol. 6, pp. 5445-61.

690 24. W.B. Liu, L. Chen, J.Z. Yan, N. Li, S.Q. Shi, and S.C. Zhang: *Corros. Sci.*, 2015,
691 vol. 94, pp. 114-21.
692 25. S. Yuan, X.L. Huang, D.L. Ma, H.G. Wang, F.Z. Meng, and X.B. Zhang: *Adv.*
693 *Mater*., 2014, vol. 26, pp. 2273-79.
694 26. J. Cabana, L. Monconduit, D. Larcher, and M.R. Palacin: *Adv. Mater*., 2010, vol.
695 22, pp. E170-92.
696 27. L.N. Sun, Q.W. Deng, Y.L. Li, L.B. Deng, Y.Y. Wang, X.Z. Ren, and P.X. Zhang:
697 *Electrochim. Acta,* 2016, vol. 222, pp. 1650-59.
698 28. L. Martin, H. Martinez, D. Poinot, B. Pecquenard, and F. Le Cras: *J. Phys. Chem.*
699 *C,* 2013, vol. 117, pp. 4421-30.
700 29. L.Y. Chen, J.S. Yu, T. Fujita, and M.W. Chen: *Adv. Funct. Mater.,* 2009, vol. 19,
701 pp. 1-6.
702 30. J.W. Zheng, S.C. Zhang, W.B. Liu, and Y.L. Xing: *Rare Metals,* 2011, vol. 30, pp.
703 374-79.
704 31. W.Q. Chen, W.F. Zhang, L. Chen, L.X. Zeng, and M.D. Wei: *J. Alloys Compd.,*
705 2017, vol. 723, pp. 172-78.
706 32. G.C. Yan, X.H. Li, Z.X. Wang, H.J. Guo, Q. Zhang, and W.J. Peng: *T. Nonferr.*
707 *Metal Soc.*, 2013, vol. 23, pp. 3691-96.
708 33. J.Y. Xiang, Z.W. Chen, and J.M. Wang: *Mater. Res. Bull.*, 2015, vol. 70, pp.
709 456-60.
710 34. C.Q. Zhang, J.P. Tu, X.H. Huang, Y.F. Yuan, X.T. Chen, and F. Mao: *Cheminform*,
711 2007, vol. 441, pp. 52-56.

712 35. R. Chen, Y. Wang, Y.N. Nuli, Y. Yu, P.F. Gao, Q. Chen, L.M. Wei, N.T. Hu, Z.
713 Yang, R.G. Gao, L.L. Zhang, and Y.F. Zhang: *Sci. China-Technol. Sc.*, 2014, vol. 57,
714 pp. 1073-76.
715 36. S. Grugeon, S. Laruelle, R. Herrera-Urbina, L. Dupont, P. Poizot, and J.M.
716 Tarascon: *J. Electrochem. Soc.*, 2001, vol. 148, pp. A285-92.
717 37. J.Y. Xiang, J.P. Tu, Y.F. Yuan, X.H. Huang, Y. Zhou, and L. Zhang: *Electrochem.*
718 *Commun*., 2009, vol. 11, pp. 262-65.
719 38. M.V. Reddy, T. Yu, C.H. Sow, Z.X. Shen, C.T. Lim, G.V. Rao, and B.V.R.
720 Chowdari: *Adv. Funct. Mater.*, 2007, vol. 17, pp. 2792-99.
721 39. J.S. Cho and Y.C. Kang: *Small*, 2015, vol. 11, pp. 4673-81.
722 40. S. Grugeon, S. Laruelle, L. Dupont, and J.M. Tarascon: *Solid State Sci*., 2003, vol.
723 5, pp. 895-904.
724 41. S. Liu, H.Y. Hou, X.X. Liu, J.X. Duan, Y. Yao, and Q.S. Liao: *Ionics*, 2017, vol.
725 23, pp. 1075-82.
726 42. S. Laruelle, S. Grugeon, P. Poizot, M. Dolle, L. Dupont, and J.M. Tarascon: *J.*
727 *Electrochem. Soc.*, 2002, vol. 149, pp. A627-34.
728 43. M. Uysal, T. Cetinkaya, A. Alp, and H. Akbulut: *J. Alloys Compd*., 2015, vol.
729 645, pp. 235-42.
730 44. B.O. Jang, S.H. Park, and W.J. Lee: *J. Alloys Compd.,* 2013, vol. 574, pp. 324-30.
731 45. W.B. Liu, X. Chen, P. Xiang, S.C. Zhang, J.Z. Yan, N. Li, and S.Q. Shi: *Nanoscale*,
732 2019, vol. 11, pp. 4885-94.
733 46. D. Aurbach, B. Markovsky, M.D. Levi, E. Levi, A. Schechter, M. Moshkovich,

734 and Y. Cohen: *J. Power Sources*, 1999, vol. 81, pp. 95-111.